Modeling of 6.1Å Family Strained Layer Superlattice Structures

Jeffrey Simon

Krishna Infrared Detector Laboratory – Department of Electrical and Computer Engineering

Professor Sanjay Krishna (Advisor)
Professor Betty Lise Anderson

Defense: 5 November 2019
Submitted: 25 November 2019

Abstract

Infrared detection and imaging in the mid-wave and long-wave infrared spectrum has well-established applications in space, defense, and environmental monitoring and is an emerging tool for researchers in medicine. Only a few types of material systems are suitable for creating photodetectors that absorb the appropriate wavelengths including the HgCdTe, the gold standard. Antimonide-based superlattice structures, consisting of thin, alternating layers of InAs, GaSb, AlSb, and InSb, are a promising alternative with theoretical predictions of performance better than the gold standard. The material composition and layer thickness in superlattices can be tuned allowing for the optimization of the structure. Furthermore, many different combinations of layer widths and material compositions can produce materials with absorption in the same wavelength range. The tunability increases the potential of antimonide-based superlattice detectors but also increases the complexity. Therefore, a fundamental understanding of the material properties must be realized through quantum-mechanical modeling.

In this research, the band structure and optical properties were explored using the 8-band k·p model. The commercially available software Nextnano3 was used to apply the 8-band k·p model to calculate the band structure of superlattice structures and custom Python scripts were used to calculate the optical absorption spectrum based on the methods of Livneh et al. However, there still exists an ambiguity in the parameters used in the k·p model requiring the optimization of parameters. An optimization routine was created, and a proof-of-concept was demonstrated. Use the developed modeling infrastructure, the k·p parameters can be tuned based on experimental results. Subsequently, the model can be used to predict and optimize the properties of new superlattice structures.

Contents

Acknowledgements

Thank you to Professor Sanjay Krishna and the Krishna Infrared Detector (KIND) research group for support and guidance during the project. I would also like to thank Professor Chris Grein at the University of Illinois at Chicago for sharing his wisdom about modeling.

The research presented is part of a collaborative project to enhance the capabilities of antimonide based infrared detectors. Experimental data and material samples were used from the KIND research group. The development of a modeling infrastructure is intended to enhance the KIND group's material design capabilities. This work was supported by the Directed Energy–Joint Transition Office, Award N00014-17-1-2440. The work was also supported by the College of Engineering at The Ohio State University.

Introduction

Imaging in the Infrared (IR) spectrum (700nm-25um) provides unique insights about the composition of gasses in the atmosphere or distant solar systems [1], allows us to see through objects, and is used in a multitude of ways in the medical field such as diagnosing cancer and diabetes [2]. Figure 1 demonstrates how blood flow can be monitored using infrared imaging after a cold coke can is removed from the inner elbow area.

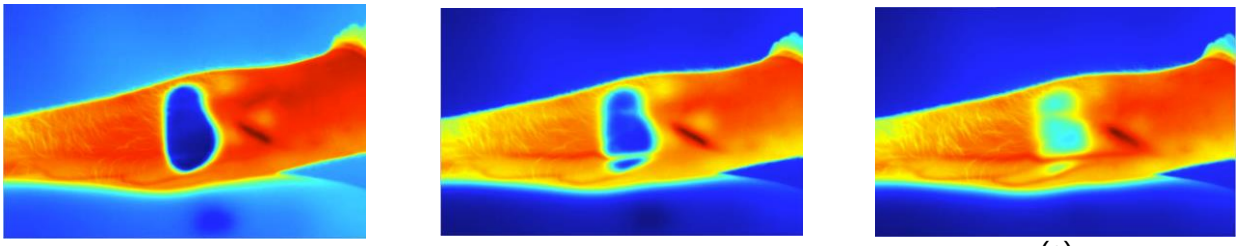

(a) (b) (c)

Figure 1: IR visualization of blood flow in an arm. The restoration of blood flow in the arm can be seen with an IR camera. A cold soda can was removed from the individual's arm just before image (a) was taken. In image (b) and (c), blood is being restored to the area evident by an increased heat signature. Image credit SKinfrared.

The performance requirements of IR photodetectors for different applications vary significantly. Detectors used for imaging in low-light environments such as in space require most of the light absorbed by the detector to be converted to an electrical signal. The noise must be minimal to prevent the signal from being obscured. In contrast, detectors used in telecommunication applications require rapid response times and a narrow spectral response as lasers light must be detected. There are many combinations of material systems and device designs available. An understanding of the application and the strengths and weaknesses of each material-device combination is necessary for determining the best choice of detector. Once a detector type and material system are chosen, the optimization of material composition and device design is necessary for the best results.

The spectrum of light that is being observed is the most important factor when choosing a material system. There are no materials that can absorb a significant amount of light across the entire IR spectrum eliminating the possibility for an ultimate material. For the Near Infrared (NIR) spectrum (750 nm – 1.4 μm), the material InGaAs is the best choice due to its absorption wavelength and properties. However, InGaAs is not an efficient absorber above 1.7 μm [1], [3]. The choice is less obvious in the Short-wave Infrared (SWIR) spectrum with wavelengths from 1.4 - 3 μm and Mid-wave Infrared (MWIR) spectrum with wavelengths from 3 – 8 μm. The II-VI material system HgCdTe, Quantum Well Infrared Photodetectors, the III-V antimonide bulk material family, and the Type-II superlattice structure created III-V antimonide family materials are all competitors [1], [3]. The following sections will discuss these material systems further with a focus on their use in IR detection.

Detector Material Structures for MWIR and LWIR

The cutoff wavelength, absorption bandwidth, absorption strength, and Quantum Efficiency (QE) are major factors when choosing a material system. The cutoff wavelength is determined by the bandgap of the material system and dictates the longest wavelength that a photodetector can detect. From a broader perspective, the cutoff wavelength determines what

detection applications the material system is suitable for. The absorption strength dictates the width of the absorber layer needed to detect the number of required photons for a specific application. From a device perspective, the absorber layer is limited to a maximum thickness to ensure most charge carriers created from the absorption of light are transported through the complete device structure enabling detection. If the absorber layer is too thick, the electron-hole pairs will be annihilated through a variety of recombination mechanisms. This is why a high absorption strength is desired. The QE of the device is a measure of the ratio of the charge carriers generated, transported through the device and collected to the number of photons absorbed. Many factors improve the QE such as increasing the material absorption, reducing the defect density, and increasing the carrier lifetime. A few prominent material systems explored for infrared detection will be introduced below.

HgCdTe Detectors

The gold standard IR detector is made from the ternary material system HgCdTe and is operated at liquid nitrogen temperatures. By changing the composition of mercury and cadmium, the bandgap can be tuned from 800 nm to 15 um [4]. Detectors made from HgCdTe were developed in the mid-twentieth century and still have the highest quantum efficiency [5]. The electrons and holes in HgCdTe have a high mobility and long lifetime leading to favorable transport properties and low dark currents [5]. The bandgap, intrinsic carrier concentration, and effective mass are just a few of the quantitative properties that can be represented by simple empirical relations based on temperature and concentration of mercury and cadmium in the material. The simple empirical relationships allow for relatively straightforward modeling and detector design [5].

Hindering the superior performance that makes this material the gold standard for IR detection, the growth of the material presents many challenges. The growth process must be controlled precisely. The HgCdTe material is grown by MBE and small variations of temperature across the wafer during growth will lead to large changes in the material structure and composition [5] [6]. This results in large variations in the band gap [7] . Different in-situ techniques are used to monitor the growth to create a more uniform structure; however, variations still exist [5].

Uniform material composition across the wafer which differs from the modeled design can be corrected by changing the operating temperature of the device; however, variations in composition across the wafer are detrimental for the consistent performance of focal plane arrays. The challenges of growing HgCdTe along with the necessity to operate the photodetector under low temperatures practically eliminates the use in broad commercial applications [1] [3]. Furthermore, the processing of HgCdTe is difficult and is not implemented commercially on a large scale. These limitations have fueled interest in other material systems and device structures for detection.

Antimonide Family Bulk Detectors

Materials in the antimonide family have an energy gap that corresponds to the Mid-Infrared (MIR) spectrum and are suitable for bulk detectors. Figure 2 shows the band lineup of the material family. Photodetectors made from InSb can be operated at room temperature unlike with other materials. InSb has a bandgap around 180 meV at room temperature which corresponds to ~7 um [8]. The electron effective mass is low, which leads to high mobility. Devices made from InSb have a high breakdown and low leakage when doped. The quality of

InSb can be made very high as it can be made in bulk. However, InSb is limited by high dark currents[8].

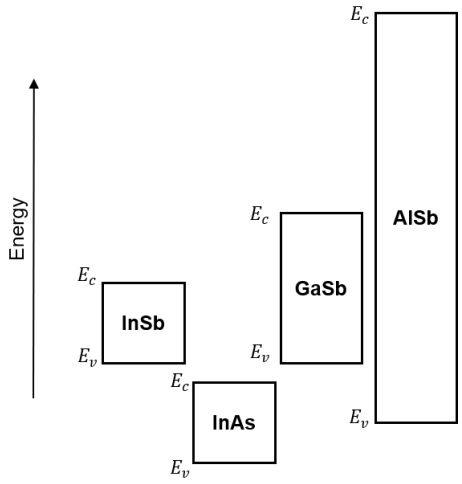

Figure 2: The band lineup of the antimonide material family.

The ternary material InAsSb has gained recent attention for the LWIR because of the small bandgap that can be tuned to correspond with absorption from 8-14 μm, and the ability to operate at room temperature [9]. However, the material properties must be refined for efficient detection. Auger recombination limits the material at high temperatures decreasing the carries that are collected, and high generation recombination rates due to thermal generation of carriers also a limitation [8]. The material is harder to grow due to the strain of growing on a lattice-mismatched material, which results in misfit dislocations. Furthermore, the device performance was worse than expected during experiments [8].

Quantum Well IR Photodetectors

IR detectors can be made from repeated quantum well structures. The quantum well structure is made from placing a narrower band gap in between materials of the wider bandgap. A potential well is created in the narrow band gap material, confining the charge carriers spatially and leading to quantized energy levels. The well thickness is on the order of tens of nanometers while the barrier thickness is on the order of tens to hundreds of nanometers in order to prevent charge carriers from neighboring wells from interacting [10]. Detectors that utilize this method are called Quantum Well IR Photodetectors (QWIPS). QWIPs are typically made of GaAs/AlGaAs layers with AlGaAs acting as the barrier and GaAs acting as the well. The absorption wavelength can be tuned by adjusting the layer thicknesses or barrier height by adjusting the composition of AlGaAs [10].

There are several limitations of QWIPs that have prevented large scale success; most limitations arise from the confined nature of charge carriers. The absorption spectrum is narrow for QWIPs due to the reliance on quantum confinement to create energy states [3]. Furthermore, the absorption is low due to a low density of states and the limited angle at which the material structure can accept light. To increase absorption, a diffraction grating is required to be fabricated on top of the detector [11]. Low mobility occurs because excited charge carriers in the QWIP structure are required to tunnel across barriers to be collected. A few flavors of QWIPs are designed to mitigate this problem by creating a continuum of states, a miniband, in

which excited charge carriers can travel [10]. All of these factors lead to a complex device to fabricate and low quantum efficiencies from 10-17% [10]. With the increasing possibilities from incorporating quantum structures into detectors, the complexity increases without significant benefit [12].

Type-II Superlattice Detectors

Superlattices consist of alternating layers of material as QWIPs do; however, the barrier layer is much thinner. The band lineup of Type-II superlattices is different, which makes unique properties accessible. A Type-II superlattice structure can be seen in Figure 3. In the Type-II band lineup, the conduction band edge of one material is lower in energy than the valence band edge of the other material. Electrons from the material with the higher energy conduction band will move to the conduction band in the material with the lower energy conduction band of the wide bandgap. A similar effect will occur with holes moving from the material with a lower energy valence band to the energy favorable state in the material with a higher bandgap. The interaction of the two materials leads to a bandgap that is smaller than the bandgap in both constituent materials [13] [14] [15].

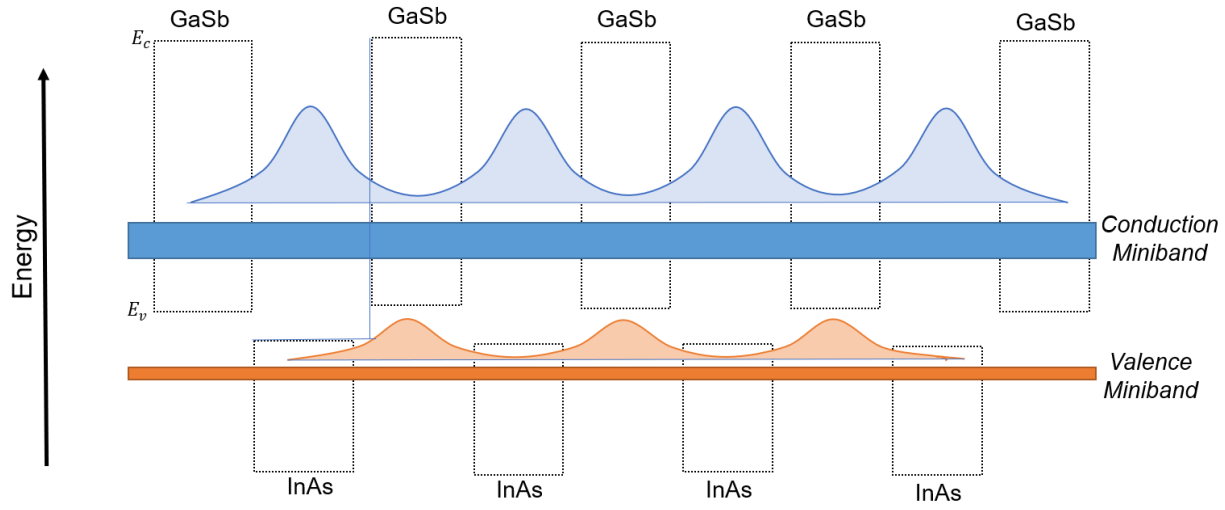

Figure 3: Type-II superlattice of alternating layers of InAs and GaSb. The first conduction miniband and first valence miniband is shown. Note that the bandgap of the minibands that are created is less than the bandgap of the constituent materials. Density of electrons and holes in each material are shown to illustrate the spatial separation of carriers in a Type-II superlattice

The electronic properties of the Type-II superlattice structure are determined by how the wavefunctions from each layer of the material interact. The thin barrier layers allow the tails of consecutive wavefunctions to overlap [16]. The overlap causes individual charge carriers to behave in a non-localized manner. In many cases, the semiconductor physics of these bands and can be modeled similarly to bulk materials (i.e. semiclassical quantities such as effective mass and mobility can be used). The dispersion relation of a superlattice can be seen in Figure 4. There exist a strong anisotropic nature to the band structure though. In the in-plane direction, the curvature of the dispersion relation is much greater than in the out-of-plane direction. This leads to a higher mobility in the in-plane direction and lower mobility in the perpendicular direction. The material is limited by defects in the crystal and Auger recombination in the LWIR spectrum, both leading to shorter carrier lifetimes affecting the transport properties [8].

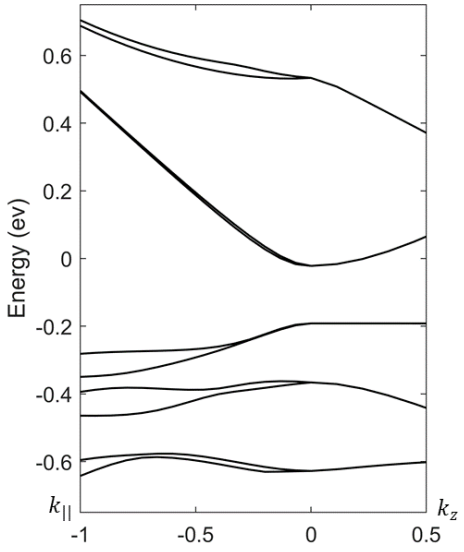

Figure 4: The dispersion relation of a 13/7 InAs/GaSb superlattice structure around the zone center

The optical properties of antimonide-base superlattice structures strengthen their ability to perform as IR detectors. Unlike with QWIPs, superlattices can absorb a broad spectrum of light because the charge carriers are not localized. Additionally, the material has a direct bandgap resulting in more favorable optical absorption and emission than an indirect bandgap material. The strength of the optical absorption depends strongly on the spatial overlap of the conduction band and valence bands. The larger spatial overlap leads to stronger absorption. The bandgap, and thus, the absorption wavelengths can be tuned by adjusting the layer widths allowing for absorption in the MIR to LWIR spectrums. Additionally, there are many layer combinations available for a specific wavelength. For the case of the InAs/GaSb superlattice, increasing the InAs layer width results in a longer cutoff wavelength and decreasing the GaSb width leads to a shorter cutoff wavelength [12].

Antimonide-based superlattice materials have a large potential for IR detection applications and require further understanding and development. The focus of the thesis will be on modeling the optical properties of this novel material system.

Outline

The next section will discuss some qualitative aspects of modeling the band structure of the superlattice materials. It will include a discussion of modeling techniques to explore the differences between first-principles and second-principles modeling and introduce a criterion for model selection. The Theoretical Approach section will discuss the mathematical basis of the chosen model and include the steps from determining optical properties from the knowledge of the band structure. The Modeling Infrastructure section will discuss the band structure modeling software, the calculation of optical properties, and the optimization method for tuning material parameters from experimental results. In the Research Outcomes section, the modeling data will be presented along with parameter optimization results for one structure. The paper will be concluded by a Future Considerations section discussing future work and the impact of the modeling work on the scientific community as well as the impact of IR detection on society.

Band Structure Modeling Overview

This section will discuss the qualitative aspects of modeling material structures. It starts by discussing the importance of superlattice structures. The fundamental types of modeling for determining the electronic properties of materials will be reviewed with a discussion of the physical nature and pros and cons. The 8-band k·p model, which was chosen based on the modeling requirements, will be introduced

Importance

Material modeling is an important aspect of experimental design when it comes to choosing what superlattice structure to use to obtain desired properties in the photodetector device. Modeling the material structure is much less time consuming and cheaper than growing the material to determine electronic and optical properties. It is oftentimes cost-prohibitive to grow a large quantity because the wafers are expensive and the cost to run a molecular beam epitaxy reactor is high.

In addition to the convenience of applying material modeling to device design, modeling introduces avenues to create and explore theories in device physics. For example, modeling enables recombination mechanisms to be understood. Grein et al. explored how to reduce the high Auger recombination rate that plagues LWIR superlattice photodetectors [17]. Klipstein et al. recently modeled generation-recombination lifetimes [18].

Considerations in Model Selection

The tradeoff between computation time and accuracy is the primary consideration when choosing a modeling method. In each theoretical model, different approximations can be made to reduce computation time. However, approximations usually reduce accuracy. There are two major classifications of models: first-principles and second-principles. The classification of these models will be introduced in the context of modeling semiconductor structures. A first-principles model computes the electronic structure of a material by combining the constituent atoms in a way that reduces the potential energy using only knowledge of atomic number and energy orbitals. A first-principles model specifically accounts for the wavefunctions corresponding to the energy levels of each atom and combines them in such a way that determines the generalized wavefunction of the material allowing for the electronic structure to be calculated.

Compared to a first-principles model, a second-principles model utilizes the parameters of the constituent atoms or materials to calculate the electronic structure of a semiconductor structure. A first-principles model is generally more computationally complex taking more time. However, it is commonly used when a strong physical understanding is necessary. A second-principles model is generated based on physical principles; however, the parameters are found by comparing model results to experimental data. The most robust second-principles modeling provides accurate prediction across semiconductor structures that have widely varying layer widths and materials.

Many different models have been used to calculate the band structure of Type-II superlattice structures including tight-binding [19] [20], density functional theory [21][22], pseudopotential [23] 8-band k·p [24] [25] [17], 14-band k·p [26], and 18-band k·p [27]. Tight-binding, density functional theory, and pseudopotential approaches explore the interactions between the electron cloud of neighboring atoms. These can be implemented using a first-

principles or second-principles approach. The k·p model takes a more macroscopic approach calculating the interactions between neighboring layers of material and is only implemented in a second-principles approach. See Smith and Mailhiot's paper for a more complete review of modeling techniques [28].

Model Selection – 8-Band k·p

The goal of the present research was to design a modeling infrastructure to accurately predict the absorption spectrum generated from interband transitions in antimonide-based Type-II superlattice structures. This application dictates the number of bands and the range of k-space that must be modeled accurately. It is also important for the simulation to not take extended amounts of time so that modeling can be done on a more rapid basis and does not require extensive computing resources.

An 8-band k·p model (a type of seconds principles model) was chosen to cut down on the computation cost. The selection of a model that only calculates 8-bands decreases the dimensionality of the Hamiltonian that must be solved speeding up the computation time. The lower computational cost makes it practical to optimize the parameters in the model using experimental data. This is necessary for producing accurate calculations.

For the modeling of a Type-II superlattice, which has a direct bandgap, the most frequent optical transitions occur at or close to the center of the Brillouin. Furthermore, the strong curvature of the conduction band also that the energy transitions in the relevant IR optical spectrum occur around the zone-center. Therefore, an accurate computation of band structure near the gamma point is necessary for calculating an accurate absorption spectrum. Computing the band structure accounting for the interaction of 8-bands provides an accurate enough band structure around the zone center for the application [17] [24] [29].

Theoretical Approach

Two important theories are applied when modeling the optical absorption of a new material structure from the parameters of the constituent materials. The first is the application of k·p theory, which is used to model the band structure of a material. The second theory describes the relationship between the band structure and optical absorption. Both will be discussed in the following sections.

K·P Theory for Superlattice

The 8-Band k•p method models the band structure of a material system using the parameters of the constituent materials. The model accounts for the interactions of the spin-up and spin-down components of three valence bands and one conduction band of the constituent materials [24] [30] [31]. This method is based on the Schrodinger Equation and Lowdin's perturbation theory. Through applying boundary conditions and different wave propagation methods, a matrix equation is created representing the interactions. The matrix can be solved for wavefunctions and energies providing the fundamental dispersion relations important to semiconductor modeling.

The following sections will discuss each major part of the theory. A general single-band k·p theory will be presented first. Then, the 8-band model will be introduced. Note that there are a few different ways to go about formalizing the theory. The approach presented here will be based on the Burt-Forman theory. Forman formulated the Hamiltonian [32] [33] while Burt developed an envelope function approach to apply the model to nanostructures [34] [35]. This model will be mainly described in a similar manner as Stefan's Birner's thesis but will include a few more fundamental details [29].

Single-band k·p

The single-band k·p theory is the basis for the more complicated 8-band method. The following explanation will be based on the discussions from Chuang's book [36]. The eigenfunctions of a crystal structure in which a unit cell is repeated are represented in the form of Bloch functions as:

$$\psi_{n\boldsymbol{k}}(\boldsymbol{r}) = e^{ik\cdot r}u_{n\boldsymbol{k}}(\boldsymbol{r}) \qquad (1)$$

The wavefunction (eq. 1) consists of two components, a phase component, $e^{ik\cdot r}$, and a complex-valued function, $u_{n\boldsymbol{k}}(r)$. The function $u_{n\boldsymbol{k}}(r)$ is described by:

$$u_{n\boldsymbol{k}}(\boldsymbol{r}+L) = u_{n\boldsymbol{k}}(\boldsymbol{r}) \qquad (2)$$

and has a periodicity of L, the same as the unit cell in the crystal.

The Hamiltonian is an operator that is used to calculate an eigenenergy from an eigenstate. The Hamiltonian varies for each k-point. A specific eigenvalue and eigenfunction is the solution to the eigenvalue problem:

$$\left[\frac{p^2}{2m_0} + \mathrm{V(r)}\right]\psi_{n\boldsymbol{k}}(\boldsymbol{r}) = E_n(k)\psi_{n\boldsymbol{k}}(\boldsymbol{r}) \qquad (3)$$

and is found by diagonalizing the Hamiltonian matrix for the specific k-point. After solving the eigenvalue problem at all k-points, a description of the band structure has been found. Eq. 3 is the single-band eigenequation created by applying the Hamiltonian to the Bloch function. $E_n(k)$ is the eigenvalue and $\psi_{n\boldsymbol{k}}(\boldsymbol{r})$ is the eigenfunction.

When the Bloch function from eq. 1 is inserted, the eigenvalue equation takes the form of:

$$\left[\frac{p^2}{2m_0} + \frac{\hbar\, k\cdot p}{m_0} + \frac{\hbar^2 k^2}{2m_0} + \mathrm{V}(\mathbf{r})\right] u_{n\boldsymbol{k}}(\boldsymbol{r}) = E_n(k) u_{n\boldsymbol{k}}(r) \qquad (4)$$

When $k = 0$, the eigensystem can be simplified as eq. 5. This equation is reduced to

$$H_0 u_{n\boldsymbol{0}}(\boldsymbol{r}) = E_n(k) u_{n\boldsymbol{0}}(\boldsymbol{r}) \qquad (5)$$

where H_0, the Hamiltonian for $k = 0$, is defined as:

$$H_0 \equiv \frac{p^2}{2m_0} + \mathrm{V}(\mathbf{r}) \qquad (6)$$

When $k \neq 0$ the Hamiltonian can be written in terms of H_0 as:

$$\left[H_0 + \frac{\hbar\, k\cdot p}{m_0} + \frac{\hbar^2 k^2}{2m_0}\right] u_{n\boldsymbol{k}}(\boldsymbol{r}) = E_n(k) u_{n\boldsymbol{k}}(\boldsymbol{r}) \qquad (7)$$

Lowdin's perturbation theory can be applied to determine the eigenvalues and eigenstates at $k \neq 0$. Lowdin's perturbation theory divides the bands into two classes: the first class consists of the bands that are being solved for and the second consists of every other bands. The first class consist of just one band for the single-band case. The resulting energies are:

$$E_n(\boldsymbol{k}) = E_n(0) + \frac{\hbar^2 k^2}{2m_0} + \frac{\hbar}{m_0}\boldsymbol{k}\cdot p_{nn} + \frac{\hbar^2}{m_0^2}\sum_{n'\neq n} \frac{|\boldsymbol{k}\cdot p_{nn'}|^2}{E_n(0) - E_{n'}(0)} \qquad (8)$$

Lowdin's perturbation theory accounts for interactions from the bands in the second class through a sum term. As the energy of the other bands become further separated from the band that is being modeled, the denominator of the sum term decreases indicating remote bands have negligible effects of the band structure. The resulting eigenfunctions are:

$$u_{n\boldsymbol{k}}(\boldsymbol{r}) = u_{n0}(\boldsymbol{r}) + \frac{\hbar}{m_0}\sum_{n'\neq n} \frac{\boldsymbol{k}\cdot p_{nn'}}{E_n(0) - E_{n'}(0)} \equiv \sum_{n'} a_{n'} u_{n'0}(\boldsymbol{r}) \qquad (9)$$

Note that $u_{n\boldsymbol{0}}(r)$, the eigenfunction for band n at $k = 0$, for all n from a set of basis functions for solving the eigenvalue equation.

Before continuing to the multiband k·p model, it is important to note that the Hamiltonian used above does not contain all of the possible interactions in the band that will be accounted for in the 8-band model. This simplification was used for instructive purposes. Other interactions between bands that will be accounted for in the 8-band model, like spin orbit coupling, cannot be represented in the single-band model.

8-Band K·P Introduction

The difference between the single-band k·p model and a multi-band k·p model is that the interband interactions are accounted for with higher accuracy resulting in a more physically

realistic model. With Lowdin's perturbation theory above, two classes of bands were considered. One class consisted of the single-band that was being modeled, the other class accounted for every other band that had interactions with the first band. The 8-band model accounts for the interactions that take place between the bands in the first class. These interactions are modeled more accurately than how it was modeled in the single-band case, by excluding it from the desired class and accounting for it with a single interaction term.

As a consequence of the careful selection of the 8-bands that will be used in the model, the excluded bands, which belong to the second class under Lowdin's perturbation theory, have a large energy difference from the bands that are modeled in the primary class. The larger gap in energy decreases the interactions according to the perturbation theory justifying neglecting the second class of bands in further calculations [37]. The exclusion of these bands provides a natural limit for the number of eigenfunctions that will be used as basis functions when calculating a solution for the eigenvalue equation. A limit to the number of basis functions, when determined from the Lowdin perturbation term, was not implicit in the single-band model.

8-band Theoretical Approach

The formalism for developing the 8-band model is very similar to the single-band model and will be reviewed below following the description in Stefan Birner's thesis [29]. Compared to the single-band Hamiltonian, a Hamiltonian representing spin orbit interactions between bands is included in the eigenvalue equation:

$$[\boldsymbol{H}_0 + \boldsymbol{H}_{so}]\psi_{n\boldsymbol{k}}(x) = E_n(k)\psi_{n\boldsymbol{k}}(x) \quad (10)$$

where the Hamiltonian at $k = 0$ (the unperturbed Hamiltonian), $\boldsymbol{H}_0$, and the spin-orbit Hamiltonian, $\boldsymbol{H}_{so}$**,** are described as:

$$\boldsymbol{H}_0 = \frac{p^2}{2m_0} + \mathrm{V(x)} \quad (11)$$

$$\boldsymbol{H}_{so} = \frac{\hbar^2}{4m_0^2c^2}(\sigma \times \nabla V) \cdot \boldsymbol{p} \quad (12)$$

Substituting the Bloch function, described in eq. 1, into the eigenvalue equation we arrive at:

$$\left[\boldsymbol{H}_0 + \boldsymbol{H}_k + \boldsymbol{H}_{k\cdot p} + \boldsymbol{H}_{so}\right] u_{n,k}(x) = E_n(k)\, u_{n,k}(x) \quad (13)$$

$\boldsymbol{H}_0$ and $\boldsymbol{H}_{so}$ are defined in eq. 11 and eq. 12. The effective mass Hamiltonian, $\boldsymbol{H}_k$, and the k·p Hamiltonian, $\boldsymbol{H}_{k\cdot p}$ are defined as:

$$\boldsymbol{H}_k = \frac{\hbar k^2}{2m_0} \quad (14)$$

$$\boldsymbol{H}_{k\cdot p} = \frac{\hbar}{m_0} k \cdot p \quad (15)$$

The Hamiltonians are formulated based on a particular set of Bloch functions that can be determined with symmetry operations through group theory and are:

$$|\mathrm{S}\uparrow\rangle,\ |\mathrm{S}\downarrow\rangle,\ |\mathrm{X}\uparrow\rangle,\ |\mathrm{X}\downarrow\rangle,\ |\mathrm{Y}\uparrow\rangle,\ |\mathrm{Y}\downarrow\rangle,\ |\mathrm{Z}\uparrow\rangle,\ |\mathrm{Z}\downarrow\rangle \quad (16)$$

The angular momentum basis functions are defined in a spherical basis and are similar to the atomic functions for the solution of the quantum mechanical hydrogen atom problem. The

functions X, Y, and Z are p-like states and represent the valence band while the S function is an s-like state. The up and down arrows represent upward and downward spins.

When solving for structures with heterojunctions as will be necessary for the case of a superlattice, the Bloch basis functions must be represented in terms of 8 envelope function each corresponding to a Bloch state.

To solve the eigenvalue problem, first the solutions are found at $k = 0$ in terms of the Bloch basis functions. Similar for the single-band case, the matrix equation evaluated at the desired $k \neq 0$ points in terms of the u_{n0} states. The solution takes on the form:

$$u_{n\boldsymbol{k}}(x) = \sum_{j=1}^{8} a_j(\boldsymbol{k}) u_{j0} \qquad (17)$$

Interface Matrix

When applying the 8-band k·p model to Type-II superlattice structures, there is a debate about the best way to model the interface between two materials. When a superlattice is grown, a thin layer (0.5ML-1.5ML) of material is intentionally formed at the interface to help balance strain. For example, in an InAs/GaSb superlattice material, a layer of InSb will be included in each period. Some research groups model it as thin layer of material as a bulk material [38] [39], while others use an interface matrix [25] [40]. The groups that model the interface layer as a bulk material arbitrarily adjust the interface width until the model produces results consistent with the experiment. For this research, the interface matrix representation was selected according to Livneh et al., who argued that the interface layer is more physically accurate and provides a more consistent treatment across different superlattice structures.

Strain

Strain is introduced in a superlattice structure because layers of material at different lattice constants are grown on top of each other. The materials are either compressed or expanded in the in-plane direction. These mechanical forces change the band structure of the constituent materials, particularly the splitting of the heavy hole and light hole bands. If a bulk material is compressed, the heavy hole band will have a higher energy than the light hole band. If the material is under tension, the light hole band will have a higher energy than the heavy hole band [28].

In the model of the superlattice, strain is typically calculated according to the lattice mismatch between the substrate and the material layer. The change in material width and band structure of each material under strain is calculated. Subsequently, the 8-band model is then applied [29] [37].

Optical Absorption Theory

Optical absorption is represented using the equation:

$$I(\lambda) = I_0(\lambda) e^{\alpha(\lambda) L}$$

Where L is the distance that light of wavelength λ has propagated through the material. I_0 is the intensity of light at $L = 0$ and I is the intensity at position L. The absorption coefficient, α, describes the propagation distance through the material at which incident light intensity is reduced by a factor of $1/e$.

Optical theory for semiconductor structures relies on the knowledge of the set of wavefunctions and energies of each calculated k-point for the states that are likely to be involved in optical transitions. For an incident photon to create an electron pair, two quantities must be conserved. First, the momentum must be conserved. Because the momentum of a photon is negligible and the probability of a phonon exchanging momentum in the process is low, the only transitions that will be considered will be between states that are at the same k-point in different bands. The second quantity that must be conserved is energy. The photon must provide the energy differences between the states that will interact to create an optical transition to be absorbed. Generally, a photon with a higher energy than the energy difference between the states can still be absorbed, but this will not be considered in the modeling. The conservation of momentum and energy limit the possible transitions that must be accounted for.

Applying the time-dependent perturbation theory, the optical transition rates or oscillator strengths can be found. Combining the oscillator strengths with the occupancy of states, the probability of a transition occurring can be found. Finally, the quantities must be normalized to calculate the absorption spectrum. The following discussion on the calculation of the optical absorption will be based on Livneh et al. [30] who modified the theory of Gershoni et al. to apply to model superlattice structures [41].

The Fourier expansion technique that is applied by Livneh et al. will first be introduced in the next section followed by the derivation of oscillator strength and absorption coefficient in the following sections.

Fourier expansion

The wavefunction, in the basis of zone-center Bloch envelope-functions of the reference crystal, is described by:

$$\psi_c(z) = \sum_{n=1}^{8} F_n(z) u_{n0}(\boldsymbol{r}) \qquad (18)$$

$F_n(z)$ describes a Fourier transform of defined in eq. 19 and eq. 20.

$$F_n(z) = \sum_j F_n(j) \phi_j(z) \qquad (19)$$

$$\phi_j(z) = \frac{1}{\sqrt{L}} e^{i \frac{2\pi}{L} jz} \qquad (20)$$

Where L is the length of a superlattice period. In the work of Linvneh et al., the Hamiltonian is solved using a modified Fourier transform with an extra exponential term adding a phase q_z in order to satisfy Bloch's theorem. The extra phase factor is unnecessary for optical calculations because it will later be canceled out by the addition of the exact opposite phase when computing the optical matrix element. There is, therefore, no reason to include the phase factor q_z in this derivation. Additionally, in the present calculations, all components of the complete Discrete Fourier Transform were used instead of restricting the set of Fourier components to the first Brillouin zone as Livneh et al. did. This will invalidate some approximations but did not cause complications.

Oscillator strength

The oscillator strength describes the relationship between two states in the context of optical absorption or emission. The higher the oscillator strength, the more likely it is that a photon can be absorbed or emitted given the transition is between states with the same crystal

momentum vector. The first step for the calculation of the oscillator strength from the band structure is calculating the optical matrix element.

The matrix element is calculated according to the result of the time-dependent perturbation theory, Fermi's golden rule:

$$M_{v,c} = \left\langle \psi_c(r) | \hat{e} \cdot \frac{\hbar}{i} \nabla | \psi_v(r) \right\rangle \qquad (21)$$

Inserting the wavefunction into eq. 18 results in the summation across Fourier components and Bloch state:

$$M_{v,c} = \sum_{n,n'=1}^{8} \sum_j \sum_{j'} F_{n,j}^{c*} F_{n',j}^{v*} \int \phi_j^*(z) u_n^*(\boldsymbol{r}) \hat{e} \cdot \frac{\hbar}{i} \nabla \phi_{j'}(z) u_{n'}(\boldsymbol{r}) d^3r \qquad (22)$$

Expanding the integral yields:

$$I = \int \phi_j^*(z) \phi_{j'}(z)\, u_n^*(\boldsymbol{r}) \hat{e} \cdot \frac{\hbar}{i} \nabla\, u_{n'}(\boldsymbol{r}) d^3r + \int \phi_j^*(z)\, u_n^*(\boldsymbol{r}) u_{n'}(\boldsymbol{r}) \hat{e} \cdot \frac{\hbar}{i} \nabla\, \phi_{j'}(z)\, d^3r \qquad (23)$$

The first integral can be simplified by applying separation of variables and substituting ϕ from eq. 20:

$$I = i\, P \frac{m_0}{\hbar} \delta_{jj'} \sum_{i=X,Y,Z} \left[e_i \sum_{k=\uparrow,\downarrow} \left(\delta_{n,S_k} \delta_{n',i_k} - \delta_{n,i_k} \delta_{n',S_k} \right) \right] \qquad (24)$$

The second integral vanishes for in-plane polarization.

The oscillator strength is the magnitude squared of the matrix element:

$$\boldsymbol{S_{v,c}} = \left| \boldsymbol{M_{c,v}} \right|^2 \qquad (25)$$

Substituting the optical matrix element:

$$S_{v,c} = \left(P \frac{m_0}{\hbar} \right)^2 \left| \sum_j \sum_{i=X,Y,Z} e_i \sum_{k=\uparrow,\downarrow} \left(F_{S_k,j}^{c*} F_{i_k,j}^{v} - F_{i_k,j}^{c*} F_{S_k,j}^{v} \right) \right|^2 \qquad (26)$$

Absorption Spectrum

The absorption is calculated by summing the differentials for each transition between k-points described by:

$$\delta\alpha(E)\Delta E \propto \frac{1}{E} \Delta N\, S(E)\, f_{vb}(k)(1 - f_{cb}(k)) \qquad (27)$$

Note that the absorption differential does not have an absolute magnitude. The absorption is normalized later. The absorption coefficient is a representation of the power loss as light travels through the material, not the proportion of photons absorbed which optical transition strengths provide information on. Thus, the absorption differential for each transition is inversely proportional to the transition energy leading to the $\frac{1}{E}$ factor. The absorption differential is proportional to ΔN, correlates to the volume contained by each k-space cell and accounts for the joint density of states. Livneh et al. does not divide k-space into equal pieces requiring the use of the term [30]. However, the term will not be included in the present model because k-space is

divided into equal size pieces. The differential ΔE is the difference in transition energies across the cell in the simulation mesh. It is used in conjunction with the equation for inhomogeneous broadening (eq. 28) to specify the width of Gaussian that will be used when calculating the absorption spectrum from oscillator strengths.

The inhomogeneous broadening equation describes the broadening due to layer width variations in a quantum well [30]:

$$\Delta E_{in} = \Delta E_0 + \frac{\Delta E_0 - \Delta E_1}{\lambda_0 - \lambda_1}(\lambda_0 - \lambda) \qquad (28)$$

Essentially, it is a linear model where the broadening at λ_0 is ΔE_1 and the broadening at λ_1 is ΔE_1 are known. The wavelength λ_0 is set to be the wavelength that corresponds to the band gap and λ_1 is set to be the wavelength that corresponds with energy the transition of the second valence band to the conduction band at the zero k-point.

Femi functions with quasi-Fermi levels

The Fermi function describes the occupancy of electrons in different energy states. When the semiconductor material absorbs light, electron-hole pairs are created. They are created faster than they can recombine until a quasi-equilibrium has been reached when the high occupancy of the conduction band and lack of available electrons in the valence reduce the absorption rate to the same as the recombination rate. The quasi-equilibrium state is represented by a quasi-Fermi level that varies from the Fermi level at equilibrium. Unlike the Fermi energy, which is the same for electrons and holes, the quasi-Fermi energy level represents the extra electrons and holes during exposure to light. The extra electrons cause the conduction band quasi-Fermi level to rise while the extra holes cause the valence band quasi-Fermi energy level to decrease.

The Fermi function for the valence band, f_v, and conduction bands, f_c, are given by

$$f_v(\boldsymbol{k}) = \frac{1}{1+e^{\frac{E_v(k)-F_v}{k_b T}}} \qquad (29)$$

$$f_c(\boldsymbol{k}) = \frac{1}{1+e^{\frac{E_c(k)-F_c}{k_b T}}} \qquad (30)$$

where $E_v(\boldsymbol{k})$ and $E_c(\boldsymbol{k})$ are the energies of the valence band and conduction band, respectively, at a specific k-point. F_v and F_c are the quasi-Fermi-level of the valance band and conduction band, respectively. The larger the temperature, T, is the broader the distribution of electrons across different energies is.

Modeling Infrastructure

The modeling was conducted using the commercially available 8-band k·p program nextnano3 to solve for the electronic structure of the material and custom Python scripts to implement the optical absorption calculations. An optimization process was also implemented to tune the parameters in order for the calculated absorption spectrum to match the experimental results. The process flow is shown in Figure 5. A Python script controlled the entire process generating the input files required for nextnano3, running the nextnano3 program, extracting simulation data from nextnano3, and initiating the optical absorption calculation.

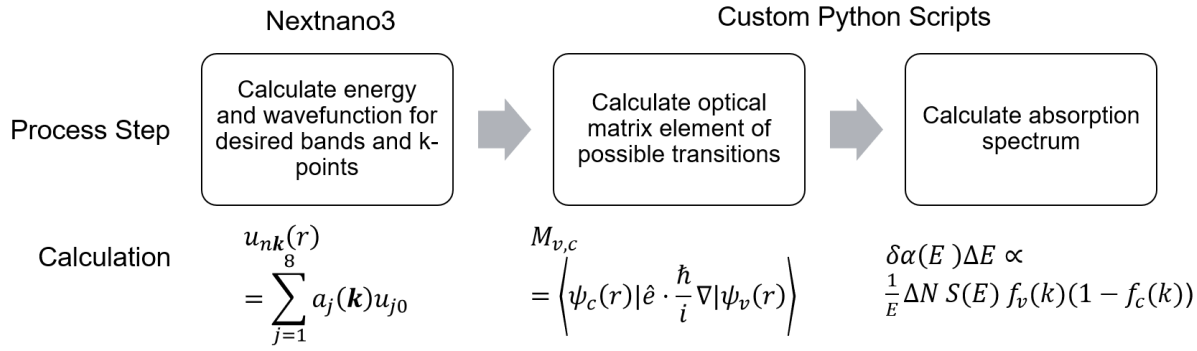

Figure 5: Modeling process used to generate an optical absorption spectrum

Nextnano3 and Nextnano++

Nextnano is a set of software for electronic modeling of semiconductor nanostructures in 1D, 2D, and 3D. It was initially developed by a research group at the Walter Schottky Institute at the Technical University in Munich and has been improved and used for multiple Ph.D. dissertations [29] [42] [43]. The code used to be made available for free to researchers around the world. More recently, nextnano became its own company and started selling a subscription to use the software [44].

Nextnano3 is the older version of the code written in Fortran while Nextnano++ is newer and is written in C++. Even though both software programs implement similar methods, the usability of Nextnano3 is much easier and is used more commonly in research publications. For the modeling infrastructure that was developed for this project, Nextnano++ was initially explored because of the updated code and the newer features available like optical calculations. However, many spurious solutions were found which resulted in complications. Additionally, the optical absorption calculations did not yield desired results after even after many tries. Therefore, Nextnano3 was the best choice.

The following sections will discuss more about Nextnano3 describing the capabilities as well as compatibility when implementing it as part of a much larger modeling infrastructure.

Theoretical Capabilities

The 8-band model that is implemented in Nextnano3 is described in the Theoretical Approach section of this paper. Nextnano's 8-band model can account for spin-orbit coupling, homogenous strain with respect to the reference crystal, and includes an interface matrix for modeling transitions from one material to another. The model is designed for general structures

and does not exploit symmetric properties of superlattices as other researchers have [28] [45]. This could lead to longer solution times for the scope of the modeling presented in this paper. However, the more complex representations could support the modeling of more complex scenarios to deeply explore the physical principles. Additionally, Nextnano3 is commonly used in the community to model superlattice structures. See [38] for a recent example.

Implementation in Modeling Suite

To run a calculation in nextnano3, an input file must be created defining the simulation scope, material structure, parameters, and other important information before running the simulation. Nextnano3 has been designed in a way so that after the input file is created, the code can be run in the command line allowing any program that can make system calls to run the software. After the simulation is run, a folder is created containing the output files. When the debugging level is increased, more detailed output files are created. For example, an output can be created that contains the complex wavefunction in terms of Bloch basis for every k-point. This allows all the data to be inputted into another modeling program to complete subsequent calculations. Also, these outputs can be especially helpful when understanding to fundamental steps of the model.

For the modeling suite, a Python program was created to interact with Nextnano3. The Python program generated an input file, ran the program with making a system call, and loaded the results for the optical computation. Nextnano3 implements a multiprocessing feature to speed up computation time during a simulation, however, there was a significant amount of the simulation that ran on a single thread. Therefore, for the highest performance, multiple nextnano3 simulations were run in parallel using a Python library

Optical Modeling Implementation

The modeling of optical properties of superlattice materials was implemented with Python code based on the work of Livneh et al. The work of Livneh also describes a method to solve the 8-band k·p model in terms of the angular momentum Bloch functions in [30]:

$$|\mathrm{S}\uparrow\rangle,\quad |\mathrm{S}\downarrow\rangle,\quad |\mathrm{X}\uparrow\rangle,\quad |\mathrm{X}\downarrow\rangle,\quad |\mathrm{Y}\uparrow\rangle,\quad |\mathrm{Y}\downarrow\rangle,\quad |\mathrm{Z}\uparrow\rangle,\quad |\mathrm{Z}\downarrow\rangle$$

The wavefunctions from Nextnano3 are calculated in terms of a basis function based on the diagonalization of the spin-orbit Hamiltonian:

$$|u_e\uparrow\rangle = |S\uparrow\rangle$$

$$|u_e\downarrow\rangle = |iS\downarrow\rangle$$

$$|u_{hh}\uparrow\rangle = \frac{1}{\sqrt{2}}|(X+iY)\uparrow\rangle$$

$$|u_{hh}\downarrow\rangle = \frac{-i}{\sqrt{2}}|(X-iY)\downarrow\rangle$$

$$|u_{lh1}\rangle = \frac{i}{\sqrt{6}}[|(X+iY)\downarrow\rangle - 2|Z\uparrow\rangle]$$

$$|u_{lh2}\rangle = \frac{1}{\sqrt{6}}[|(X-iY)\uparrow\rangle + 2|Z\downarrow\rangle]$$

$$|u_{so1}\rangle = \frac{1}{\sqrt{3}}[|(X - iY)\downarrow\rangle + |Z\uparrow\rangle]$$

$$|u_{so2}\rangle = \frac{-i}{\sqrt{3}}[|(X - iY)\uparrow\rangle - |Z\downarrow\rangle]$$

The aim of the optical modeling was to replicate Livneh's process most accurately, thus, the Nextnano wavefunctions were converted to the standard angular momentum Bloch functions with the following rotation matrix.

$$M_{conversion} = \begin{bmatrix} 1 & 0 & 0 & 0 & 0 & 0 & 0 & 0 \\ 0 & i & 0 & 0 & 0 & 0 & 0 & 0 \\ 0 & 0 & \frac{1}{\sqrt{2}} & 0 & -\frac{i}{\sqrt{2}} & 0 & 0 & 0 \\ 0 & 0 & 0 & -\frac{i}{\sqrt{6}} & 0 & -\frac{1}{\sqrt{6}} & i\sqrt{\frac{2}{3}} & 0 \\ 0 & 0 & \frac{1}{\sqrt{6}} & 0 & \frac{i}{\sqrt{6}} & 0 & 0 & \sqrt{\frac{2}{3}} \\ 0 & 0 & 0 & -\frac{i}{\sqrt{2}} & 0 & \frac{1}{\sqrt{2}} & 0 & 0 \\ 0 & 0 & 0 & \frac{1}{\sqrt{3}} & 0 & -\frac{i}{\sqrt{3}} & \frac{1}{\sqrt{3}} & 0 \\ 0 & 0 & \frac{i}{\sqrt{3}} & 0 & -\frac{1}{\sqrt{3}} & 0 & 0 & -\frac{i}{\sqrt{3}} \end{bmatrix}$$

Once the wave functions were in the correct basis, the Fourier components specified in the optical theory section were found by applying a non-uniform spacing Fourier transform. The computations described in the optical theory section was then performed.

Quasi-Fermi energy levels

The quasi-Fermi energy levels have a large ability to change the shape of the absorption curve. However, because the oscillator strengths are multiplied by a Fermi function for the valence band and for the conduction band energies, there is a clear relation to the distortion of the absorption curve due to an incorrect Fermi function. This does not mean that tuning the quasi-Fermi energy levels is trivial. In fact, it is perhaps the most difficult part in the implementation because of the possible options and that the quasi-Fermi energy levels change when input parameters are changed. Furthermore, nextnano3 does not accurately compute the Fermi levels. Through analysis of the effect of adjusting the quasi-Fermi levels on the absorption spectrum, an intuition developed to determine whether the Fermi function was incorrect. The development of this will be presented.

It is helpful to start by examining the absorption spectrum when the Fermi levels are not accounted for. The multiplication of the Fermi function suppresses the strengths of absorption related to some transitions. Figure 6(a) shows the effect of only multiplying the strengths by the

valence band Fermi function for various quasi-Fermi levels accounting for the occupancy of the valence band. Figure 6(b) shows a similar representation for the conduction band.

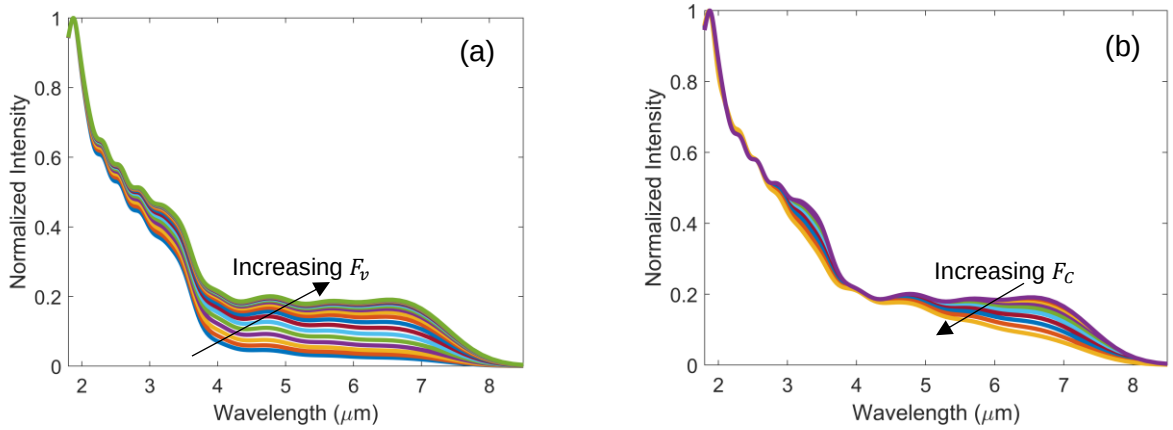

Figure 6: The variation of the quasi-Fermi level of the valence band (a) and the conduction band (b) on the shape of the optical absorption spectrum.

Increasing the quasi-Fermi level for the valence band leads to a more defined cutoff at the energy gap and a less steep slope in the lower wavelength range of the absorption spectrum. This is a trivial result. When the quasi-Fermi energy is lowered, there are more electrons available in the lower valence bands relative to the higher valence bands increasing the absorption rate of the lower valence bands relative to the upper valence band.

Increasing the Fermi level of the conduction band has an opposite effect resulting in a less defined cutoff near the wavelength associated with the band gap and a steeper slope in the low wavelength range of the absorption spectrum. This is a trivial result because as electrons begin to fill the lower energy positions in the conduction bands, electrons from the valence band must transition to a higher energy. The oscillator strength as k moves away from the gamma point also decreases.

In the calculations, the quasi-Fermi level was set relative to the conduction band energy and was chosen to enhance the tail near the cutoff wavelength. The tail of the absorption spectrum in experimental results is correlated with the band gap as can be confirmed by PL measurements and modeling. This absorption cutoff is a significant factor in material and device design deeming it necessary to modify the quasi-Fermi levels of the conduction band to obtain accurate results.

Optimization Implementation

The optimization of parameters from experimental data is a key step for developing an accurate model. A description of the algorithm is given below in Figure 7. An initial parameter set is passed in. This is usually taken from a commonly accepted set of parameters in literature. The optimization routine is based on a gradient descent method. During each iteration, the program computes the regression of the calculated data accounting for a small increment and decrement for one parameter. The algorithm relies on parallel computing to compute the new regressions simultaneously. The algorithm then determines which parameter steps reduced the regression to create a new parameter list.

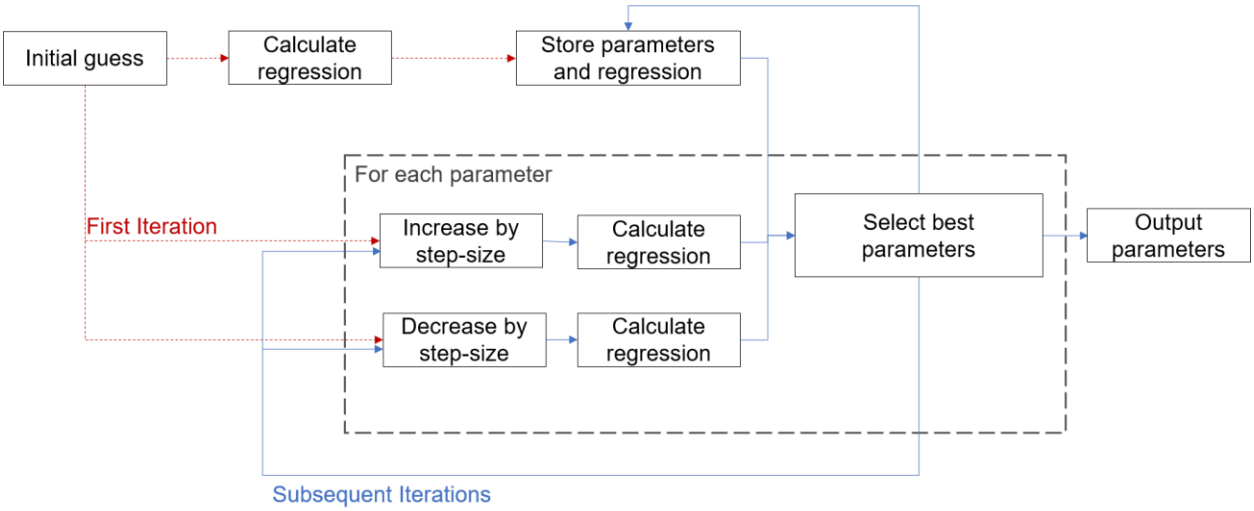

Figure 7: The optimization process in tuning material parameters from experimental data

For a given Type-II superlattice with layers made from binary materials, there are 12 material parameters that do not have values that are agreed upon in literature. This is partially because of structural variation even when growing the same structure in different MBEs and also in part due to the different approximations that are made in k·p models. For the current implementation calculations for an InAs/GaSb superlattice is optimized, six variables are being tuned: 3 are interface parameters, two are Luttinger parameters for InAs, and the last is the valence band offset of GaSb. The other 6 parameters can be approximately computed from combining well-known material parameters and small approximations [30].

Research Outcomes

The modeling infrastructure was tested through the above-mentioned optimization process tuning the material parameters so that the calculated optical absorption spectrum was consistent with the experimental absorption data. The optimization was completed for a 13/7 InAs/GaSb superlattice at 300K. It is important to note that the quality of this sample was low with a large uncertainty in period thickness. Additionally, note that some oscillatory artifacts are also present in the upper tail of the data. Therefore, the results that will be presented are intended only to test the modeling infrastructure, not to suggest a set of parameters for use in this material system.

The modeling of the optical spectrum was completed with the quasi-Fermi level of the conduction band at the conduction band edge and the quasi-Fermi level of the valence band 10 meV lower. The inhomogeneous broadening parameters that produced the best result were $\Delta E_0 = \Delta E_1 = 15$ meV. The choice resulted in equal inhomogeneous broadening across the entire spectrum.

The optimization converged after about 200 iterations. Each iteration consisted of the calculation of optical absorption with 13 different sets of parameters. The average time per iteration was 3.5 minutes when applying parallel processing using a computer with a 12-core processor. The plot in Figure 8(a) shows the experimental absorption in blue with the calculated absorption overlaid in red. Additionally, the photoluminescence spectrum was computed. The list of optimized parameters is shown in Table 1. The dispersion relation was plotted and is shown in Figure 8(b).

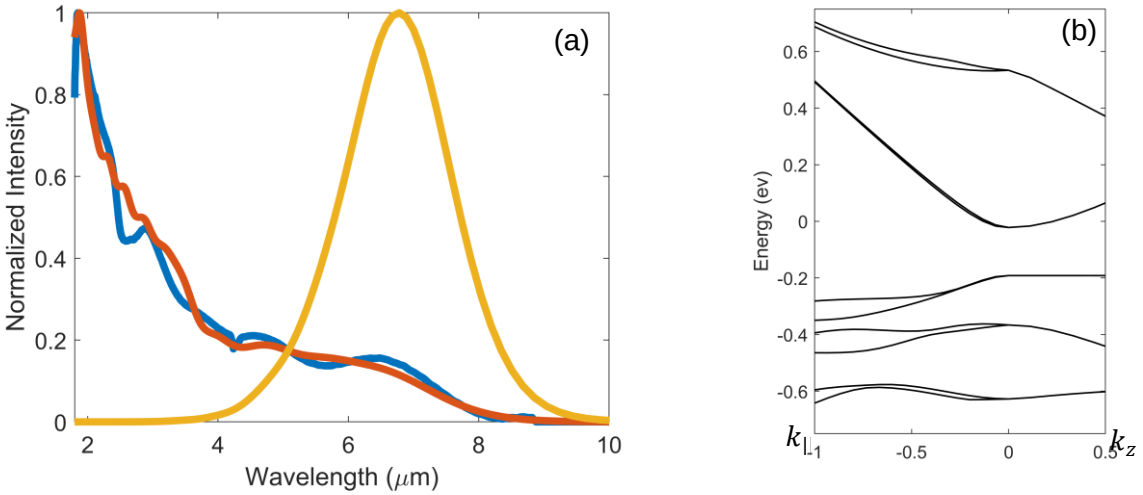

Figure 8: Optimization optical and band structure results. (a) The results of optimizing parameters to a 13/7 InAs/GaSb superlattice. The experimental absorption spectrum (blue), calculated absorption spectrum (red), and PL spectrum (yellow) are shown. (b) the dispersion relation is shown for the optimized parameters.

Table 1:Optimized parameters for 13/7 InAs/GaSb superlattice

Parameter	Value
$d_s\ (eV\ Å)$	-2.10
$d_x (eV\ Å)$	-1.44
$d_z (eV\ Å)$	1.44
$\alpha\ (eV\ Å)$	0.806
$\beta\ (eV\ Å)$	0.806
$\gamma_{1\ InAs}$	19.937
$\gamma_{2\ InAs}$	8.501
$\gamma_{3\ InAs}$	9.352
$\gamma_{1\ GaSb}$	11.99
$\gamma_{2\ GaSb}$	4.088
$\gamma_{3\ GaSb}$	5.234
InAs offset (eV)	-0.549

Comparison of Key Features

When qualitatively evaluating the fit of an optical model to experimental results, there are a few major factors that are taken into account: the absorption cutoff wavelength and shape. The absorption cutoff wavelength of the experiment should align closely with that of the model. The cutoff wavelength is a representation of the bandgap. The calculated PL intensity can also provide information on the bandgap. The decay of the right tail of the PL curve in Figure 8(a) aligns with the cutoff of the calculated absorption confirming the position of the quasi-Fermi levels were set appropriately. Otherwise, these two features would not align because the Fermi distribution would suppress the absorption near the wavelength associated with the band gap giving the appearance of a lower cutoff wavelength.

In Figure 8(a), the shape of the calculated absorption spectrum from 4-10 μm is consistent with experimental data after taking into account the artifacts. The calculated absorption in the range of 2.25-4 μm does not fit the shape as well. The peak in the experimental absorption spectrum around 3 μm is a consequence of a smaller amount of inhomogeneous broadening at that point compared to the rest of the spectrum. The optical absorption model considered inhomogeneous broadening similarly to how it would be modeled in a quantum well and only accounted for two transitions. There is no evidence it increased the model's accuracy. This method of calculating inhomogeneous broadening should be revaluated. The inhomogeneous broadening around 3 μm in the model must be decreased to account for the sharp peak.

The calculated data in the 2-3 μm range contains oscillatory artifacts because the resolution in k-space is too small. The calculated weighted Gaussian distribution for each transition are summed together to create the absorption spectrum. The gaussians must be sufficiently overlapped to produce a smooth spectrum. However, in the 2-3 μm range, there is not sufficient overlap. The centers of the neighboring gaussians are too far away creating the artifacts. Increasing the resolution in k-space as well as adjusting the inhomogeneous broadening would lead to a smoother absorption peak with a shape more consistent with the experimental spectrum.

Future Modeling Considerations

This next section will discuss possible improvements to the optical absorption model. Following there will be a discussion on wider impacts of the design as a required section for meeting capstone requirements.

Future Work

The modeling work showed high potential for obtaining results that are helpful to the scientific research community. With the improvements, the model will be able to accurately tune parameters so that nexntnano3 can provide to most accurate results for superlattice modeling.

Band structure modeling

The lack of knowledge of the Fermi level position is the largest concern about the band structure modeling component of the developed modeling infrastructure. The position of the quasi-Fermi levels was discussed in detail in the modeling infrastructure section. The shape of the absorption spectrum can be highly distorted if an incorrect value was used. Determining a more complete methodology to predict the quasi-Fermi level could improve the accuracy of the model. One possibility is to account for charge neutrality, placing the Fermi level at a position that results in an equal number of electrons and holes. Furthermore, the quasi-Fermi levels could be calculated through estimating the density of electron-hole pairs created by the absorption of light and again accounting for the density of states.

Optical Absorption Model

The optical absorption model requires tuning to produce the most accurate results. Some of the quantities used in determining the spectrum like how it accounts for inhomogeneous broadening and Fermi level position is purely empirical and has the potential to affect the exact absorption curve. A stronger physical basis to account for these parameters would lead to better results.

In the optical calculations presented in the paper, the calculated spectrum was normalized relative to itself rather than scaled according to the physical parameters. A change in overall intensity would therefore not be accounted for. This produced reasonable results but increasing the accuracy by better accounting for the physical parameters would lead to better optimization results and a more consistent set of parameters.

Optimization

The optimization was completed by comparing the calculations of an optical absorption spectrum for one material structure with its experimental results. A more robust set of parameters could be found if the optimization involved comparing the calculated absorption with the experimental absorption of superlattice structures with varying layer widths. This would decrease the possibility of overfitting the data by reducing the number of degrees of freedom.

Additionally, a more reliable optimization routine could account for more factors than only the optical absorption spectrum. The bandgap of the material could be extracted from the PL data or absorption spectrum. The computational cost of calculating the zero points in k-space is significantly quicker than calculating for all k-points. If a two-part optimization process was created with the first part accounting for the energy of transitions at the gamma point and

the second part accounting for the absorption spectrum, the optimization process would take less time.

Wider Impacts of Design

The long-term outcome of developing a modeling infrastructure is the creation of better photodetectors; thus, the following discussion will be centered around the environmental and social impacts of IR photodetectors.

Environment

The impact of the semiconductor industry on the environment is not overwhelmingly positive. The chemicals that are used carry reproductive risk and are carcinogenic leading to higher risks of non-Hodgkin's lymphoma, leukemia, brain tumors, and breast cancer for workers [46]. Furthermore, toxins are released into the air from fume hoods into the environment [47]. While one could make the argument that modeling helps reduce waste in semiconductor research and development because not as many devices need to be made, (which is a perfectly valid argument), the modeling efforts support the continued work in the semiconductor industry. Perhaps, if strong modeling tools did not exist, the semiconductor industry would not have grown this large.

Superlattices are grown in MBEs, which uses high amounts of electricity powering the many vacuum pumps to bring the chamber pressure to around 1e-10 torr. Furthermore, mining and manufacturing high purity materials that are used during growth can come at a huge cost for the environment [48].

Applications of the materials that would be modeled by the infrastructure that was developed typically are used for IR detection. Better IR detectors would advance remote sensing capability leading to better monitoring of environmental conditions across the globe from satellites. Additionally, they can be used for research applications in astronomy. Both applications could positively help the environment.

Social Issues

IR detectors are used primarily for military applications. They are used in missiles to track targets and in surveillance. In fact, a large amount of IR research is sponsored by the Department of Defense. The uses of detectors for thesis applications can provide a positive or negative impact on the world society depending on personal perspective. Additionally, scientific research on antimonide-based materials and photodetectors is limited to certain countries where the materials are available because the US government restricts the spread of technology that can be used for military applications, such as IR detectors, to other countries.

References

[1] M. N. Abedin, M. G. Mlynczak and T. F. Refaat, "Infrared detectors overview in the short-wave infrared to far-infrared for CLARREO mission," in *Infrared Remote Sensing and Instrumentation XVIII,* 2010.

[2] B. B. Lahiri *et al*, "Medical applications of infrared thermography: a review," *Infrared Phys. Technol.,* vol. 55, *(4),* pp. 221-235, 2012.

[3] A. Rogalski, "Infrared detectors: an overview," *Infrared Phys. Technol.,* vol. 43, *(3-5),* pp. 187-210, 2002.

[4] W. D. Lawson *et al*, "Preparation and properties of HgTe and mixed crystals of HgTe-CdTe," *Journal of Physics and Chemistry of Solids,* vol. 9, *(3-4),* pp. 325-329, 1959.

[5] D. R. Rhiger, "HgCdTe long-wave infrared detectors," in *Semiconductors and Semimetals* 2011.

[6] A. Rogalski, "HgCdTe infrared detector material: history, status and outlook," *Reports on Progress in Physics,* vol. 68, *(10),* pp. 2267-2336, 2005. Available: http://iopscience.iop.org/0034-4885/68/10/R01. DOI: 10.1088/0034-4885/68/10/R01.

[7] M. Razeghi and B. Nguyen, "Advances in mid-infrared detection and imaging: a key issues review," *Reports on Progress in Physics. Physical Society (Great Britain),* vol. 77, *(8),* pp. 082401, 2014. Available: https://www.ncbi.nlm.nih.gov/pubmed/25093341. DOI: 10.1088/0034-4885/77/8/082401.

[8] M. Razeghi, "Overview of antimonide based III-V semiconductor epitaxial layers and their applications at the center for quantum devices," *The European Physical Journal-Applied Physics,* vol. 23, *(3),* pp. 149-205, 2003.

[9] R. Hasegawa *et al*, "Room temperature operating InAsSb-based photovoltaic infrared sensors grown by metalorganic vapor phase epitaxy," *J. Cryst. Growth,* vol. 464, pp. 211-214, 2017.

[10] S. D. Gunapala and S. V. Bandara, "Quantum well infrared photodetector (QWIP) focal plane arrays," in *Semiconductors and Semimetals*, 1999.

[11] M. Z. Tidrow *et al*, "Device physics and focal plane array applications of QWIP and MCT," in *Photodetectors: Materials and Devices IV,* 1999.

[12] M. Razeghi and B. Nguyen, "Advances in mid-infrared detection and imaging: a key issues review," *Reports on Progress in Physics,* vol. 77, *(8),* pp. 082401, 2014.

[13] D. L. Smith and C. Mailhiot, "Proposal for strained type II superlattice infrared detectors," *J. Appl. Phys.,* vol. 62, *(6),* pp. 2545-2548, 1987.

[14] C. H. Grein, J. Garland and M. E. Flatté, "Strained and Unstrained Layer Superlattices for Infrared Detection," *Journal of Electronic Materials,* vol. 38, *(8),* pp. 1800-1804, 2009. Available: https://search.proquest.com/docview/499149429. DOI: 10.1007/s11664-009-0757-8.

[15] A. Rogalski, "Infrared detectors: an overview," *Infrared Physics and Technology,* vol. 43, *(3),* pp. 187-210, 2002. Available: https://www.sciencedirect.com/science/article/pii/S1350449502001408. DOI: 10.1016/S1350-4495(02)00140-8.

[16] D. Z. Ting *et al*, "Type-II superlattice infrared detectors," in *Semiconductors and Semimetals* 2011.

[17] C. H. Grein *et al*, "Long wavelength InAs/InGaSb infrared detectors: Optimization of carrier lifetimes," *J. Appl. Phys.,* vol. 78, *(12),* pp. 7143-7152, 1995.

[18] P. C. Klipstein *et al*, "InAs/GaSb type II superlattice barrier devices with a low dark current and a high-quantum efficiency," in *Infrared Technology and Applications XI,* 2014.

[19] R. Haydock, V. Heine and M. J. Kelly, "Electronic structure based on the local atomic environment for tight-binding bands," *Journal of Physics C: Solid State Physics,* vol. 5, *(20),* pp. 2845, 1972.

[20] Y. Wei and M. Razeghi, "Modeling of type-II InAs/GaSb superlattices using an empirical tight-binding method and interface engineering," *Physical Review B,* vol. 69, *(8),* pp. 085316, 2004.

[21] Z. Taghipour, E. Shojaee and S. Krishna, "Many-body perturbation theory study of type-II InAs/GaSb superlattices within the GW approximation," *Journal of Physics: Condensed Matter,* vol. 30, *(32),* pp. 325701, 2018.

[22] M. Caid *et al*, "Full potential study of the structural, electronic and optical properties of (InAs) m/(GaSb) n superlattices," *Computational Condensed Matter,* pp. e00394, 2019.

[23] G. C. Dente and M. L. Tilton, "Comparing pseudopotential predictions for InAs/GaSb superlattices," *Physical Review B,* vol. 66, *(16),* pp. 165307, 2002.

[24] P. C. Klipstein, "Operator ordering and interface-band mixing in the Kane-like Hamiltonian of lattice-matched semiconductor superlattices with abrupt interfaces," *Physical Review B,* vol. 81, *(23),* pp. 235314, 2010.

[25] P. C. Klipstein *et al*, "Modeling InAs/GaSb and InAs/InAsSb superlattice infrared detectors," *J Electron Mater,* vol. 43, *(8),* pp. 2984-2990, 2014.

[26] C. H. Grein *et al*, "Modeling of very long infrared wavelength InAs/GaInSb strained layer superlattice detectors," in *Materials for Infrared Detectors II,* 2002, .

[27] J. Imbert *et al*, "Electronic structure of InAs/GaSb superlattice for the modelling of MWIR pin photodiode," *Infrared Phys. Technol.,* vol. 70, pp. 81-86, 2015.

[28] D. L. Smith and C. Mailhiot, "Theory of semiconductor superlattice electronic structure," *Reviews of Modern Physics,* vol. 62, *(1),* pp. 173, 1990.

[29] S. Birner, "Modeling of semiconductor nanostructures and semiconductor-electrolyte interfaces," 2011.

[30] Y. Livneh *et al*, "k· p model for the energy dispersions and absorption spectra of InAs/GaSb type-II superlattices," *Physical Review B,* vol. 86, *(23),* pp. 235311, 2012.

[31] J. M. Luttinger and W. Kohn, "Motion of electrons and holes in perturbed periodic fields," *Physical Review,* vol. 97, *(4),* pp. 869, 1955.

[32] B. A. Foreman, "Effective-mass Hamiltonian and boundary conditions for the valence bands of semiconductor microstructures," *Physical Review B,* vol. 48, *(7),* pp. 4964, 1993.

[33] B. A. Foreman, "Elimination of spurious solutions from eight-band k· p theory," *Physical Review B,* vol. 56, *(20),* pp. R12748, 1997.

[34] M. G. Burt, "The justification for applying the effective-mass approximation to microstructures," *Journal of Physics: Condensed Matter,* vol. 4, *(32),* pp. 6651, 1992.

[35] M. G. Burt, "Fundamentals of envelope function theory for electronic states and photonic modes in nanostructures," *Journal of Physics: Condensed Matter,* vol. 11, *(9),* pp. 53, 1999.

[36] S. L. Chuang and S. L. Chuang, "Physics of optoelectronic devices," 1995.

[37] T. B. Bahder, "Eight-band k· p model of strained zinc-blende crystals," *Physical Review B,* vol. 41, *(17),* pp. 11992, 1990.

[38] M. Delmas, B. L. Liang and D. L. Huffaker, "A comprehensive set of simulation tools to model and design high-performance type-II InAs/GaSb superlattice infrared detectors," in *Quantum Sensing and Nano Electronics and Photonics XVI,* 2019.

[39] B. Satpati *et al*, "Interface analysis of InAs/GaSb superlattice grown by MBE," *J. Cryst. Growth,* vol. 301, pp. 889-892, 2007.

[40] P. C. Klipstein *et al*, "A k· p model of InAs/GaSb type II superlattice infrared detectors," *Infrared Phys. Technol.,* vol. 59, pp. 53-59, 2013.

[41] D. Gershoni, C. H. Henry and G. A. Baraff, "Calculating the optical properties of multidimensional heterostructures: Application to the modeling of quaternary quantum well lasers," *IEEE J. Quant. Electron.,* vol. 29, *(9),* pp. 2433-2450, 1993.

[42] T. Eissfeller, "Linear Optical Response of Semiconductor Nanodevices." , Technische Universität München, 2008.

[43] T. Andlauer, "Optoelectronic and Spin-Related Properties of Semiconductor Nanostructures in Magnetic Fields." 1. Aufl., Verein zur Förderung des Walter Schottky Inst. der Techn. Univ. München e.V, Garching, 2009.

[44] *Nextnano: Software for the simulation of electronic and optoelectronic semiconductor nanodevices*. Available: nextnano.de.

[45] G. Bastard, "Wave mechanics applied to semiconductor heterostructures," 1990.

[46] M. Kim, H. Kim and D. Paek, "The health impacts of semiconductor production: an epidemiologic review," *International Journal of Occupational and Environmental Health,* vol. 20, *(2),* pp. 95-114, 2014.

[47] Y. Eom *et al*, "Emission factors of air toxics from semiconductor manufacturing in Korea," *J. Air Waste Manage. Assoc.,* vol. 56, *(11),* pp. 1518-1524, 2006.

[48] A. Plepys, "The environmental impacts of electronics. going beyond the walls of semiconductor fabs," in *IEEE International Symposium on Electronics and the Environment, 2004. Conference Record. 2004*.